

Design and Objective Evaluation of Filter- and Optimization-based Motion Cueing Strategies for a Hybrid Kinematics Driving Simulator with 5 Degrees of Freedom

Patrick Biemelt, Sandra Gausemeier, and Ansgar Trächtler

Chair of Control Engineering and Mechatronics, Heinz Nixdorf Institute, University of Paderborn, Germany

Email: {patrick.biemelt, sandra.gausemeier, ansgar.traechtler}@hni.uni-paderborn.de

Abstract—Dynamic driving simulators have become a key technology to support the development and optimization process of modern vehicle systems both in academic research and in the automotive industry. However, the validity of the results obtained in simulator tests depends significantly on the adequate reproduction of the simulated vehicle movements and the associated immersion of the driver. Therefore, specific motion platform control strategies, so-called *Motion Cueing Algorithms* (MCA), are used to render the acting accelerations and angular velocities within the physical limitations of the driving simulator best possible. In this paper, we describe the design and implementation of two different control approaches for this task, using a simulator with hybrid kinematics motion system as an application example. Motivated by its unique features, an improved filter-based algorithm as well as a real-time capable optimization-based strategy following the idea of *Model Predictive Control* (MPC) are presented and discussed in detail. By means of introduced quality criteria, both algorithms are objectively compared with regard to various standard driving scenarios. These include longitudinal and lateral dynamic maneuvers to estimate the overall improvements of each MCA for interactive driving simulation. Measurement data indicate that both approaches yield an adequate control quality, however, the MPC-based algorithm better handles the kinematic constraints of the simulator due to the integration of additional model knowledge.

Keywords—Interactive Driving Simulation; Motion Cueing; Washout Algorithm; Model Predictive Control; Objective Quality Criteria.

I. INTRODUCTION

This article is based on previous work originally presented in [1]. It extends the existing results and provides a deeper understanding of the described concepts and methods.

As a consequence of the constantly increasing multifunctionality and interconnectivity of modern vehicle components and Advanced Driver Assistance Systems (ADAS), automobile manufacturers and developers are facing new technological challenges in recent years. Furthermore, topics such as e-mobility and autonomous driving bring new competitors from the information technology sector onto the market, so that shorter development cycles with simultaneously enhanced product complexities are necessary in order to maintain competitiveness. To overcome those new technological challenges, the use of interactive driving simulators, as shown exemplary in Figure 1, represents an indispensable tool to complement the conventional development process, based on physical prototypes and on-road tests, by model-based test procedures. Such virtual prototyping methods using driving simulators provide the benefit of time and cost savings, as well as safe and reproducible test environments with a high level of flexibility at the same time. For instance, varying weather and lighting conditions can be directly adapted to the test requirements in the simulated environment, which supports i.a. the



Figure 1. Interactive Driving Simulators from the Automotive Field [5][6].

development and optimization of modern headlamp systems significantly [2]. Furthermore, interactive driving simulation enables to access human-centered aspects, such as marketing, driver training and behavioral studies [3][4].

Disregarding from the particular analysis purpose, the validity of the results obtained in a virtual test drive is closely linked to the degree of immersion. Interactive driving simulation can therefore be characterized as a *Human- and Hardware-in-the-Loop* (HHIL) application whose transferability to real driving situations can only be guaranteed if a realistic driving impression is created. Hence, it is necessary to provide the human perception system with all required motion information, so-called *Motion Cues*. In addition to the acoustic, visual and haptic stimuli, also the vestibular Motion Cues, more precisely the acting translational accelerations and angular velocities of the simulated vehicle, must be generated using the motion system of the simulator. For this reason, specific Motion Cueing Algorithms are applied in order to create a driving experience that is as realistic as possible within the physical limitations of the motion system.

The most common approach for this task is the *Classical Washout Algorithm* (CWA), which was first described by Schmidt and Conrad as a motion platform control algorithm for piloted flight simulators [7]. As illustrated in Figure 2, this

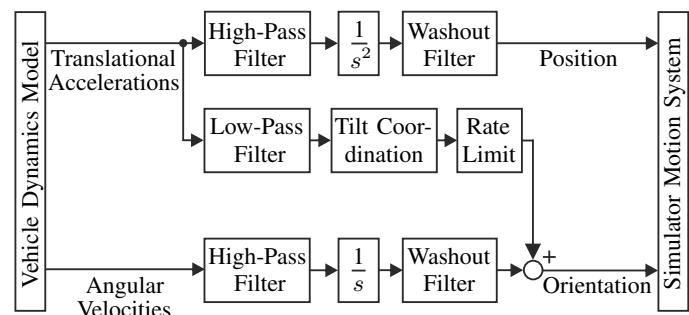


Figure 2. Scheme of the Classical Washout Algorithm [7].

MCA basically consists of a sequence of frequency divisions in order to generate suitable position and orientation reference signals for the simulator motion system. The high-frequency components of the scaled translational accelerations and angular velocities of the vehicle dynamics model are therefore separated using appropriate high-pass filters. Afterwards, these extracted components are directly integrated to a corresponding position and orientation of the driving simulator. Since the basic idea of this algorithm is to return the motion system to its neutral position after it has performed the high-frequency movements, a further high-pass filtering of the integrated signals is conducted. This is known as the *washout effect*. Due to the typically small workspace, an analog integration of the low-frequency accelerations and angular velocities would lead the motion system quickly to its physical limits and thus cannot be performed. Hence, sustained accelerations are simulated via the *tilt coordination* technique, which makes use of the gravitational force to replicate these accelerations by an equivalent rotation of the driving simulator. The corresponding rotation rate is usually limited to the perception threshold of the human vestibular system in this process, so that the rotational motion will not be realized by the driver inside the simulator.

This simple control strategy has been extensively studied and improved since its first publication, typically using hexapod-based motion systems [8][9]. As a result of this research, the filter-based MCA evolved into the standard approach in interactive driving simulation that offers major benefits in terms of transparency and traceability. Each parameter in the Classical Washout Algorithm has a clear physical meaning and a unique association to a single degree of freedom (DOF), which simplifies the tuning significantly. However, this basic idea of treating the translational accelerations and angular velocities independently results in the fact that this approach cannot be applied to every type of motion system. Otherwise, conflicting vestibular stimuli are generated under certain circumstances, e.g., if there exist interdependencies between translational and rotational DOF of the motion system like it is introduced in the next section with the ATMOS driving simulator.

In the present work, we propose an improvement of the CWA that enables a dynamic position washout to any point within the simulator workspace without considerably affecting the high-frequency motion rendering. This key feature is motivated by the considered motion system, but can also be applied to other systems, which offers general advantages for interactive driving simulation. Furthermore, the design and implementation of a real-time capable optimization-based controller is described. It contains additional information by integrating a mathematical model of the motion system, which enables an adequate planning of the simulator trajectory according to the current driving situation. The resulting control quality is evaluated by means of defined objective quality criteria, which take into account both measured and perceived quantities, including models of the human perceptual system. Based on this valuation metric, both MCA are compared using established driving scenarios from the automotive industry, as well as everyday driving maneuvers.

The rest of this paper is structured as follows: Section II provides a detailed overview of the considered motion system and analyzes its specific kinematic characteristics that have to be taken into account to ensure a realistic driving impression. Motivated by these findings, Sections III and IV present the de-



Figure 3. ATMOS Dynamic Driving Simulator.

veloped filter- and optimization-based MCA. Subsequently, the objective valuation metric and the examined driving scenarios are introduced in Section V, while Sections VI and VII finally discuss the obtained results and give concluding remarks.

II. ATMOS DYNAMIC DRIVING SIMULATOR

Figure 3 shows the Atlas Motion System (ATMOS) driving simulator that is operated at the Heinz Nixdorf Institute in Paderborn as a reconfigurable development platform, primarily for lighting-based ADAS. As illustrated, this simulator is equipped with a real vehicle chassis of a Smart Fortwo including all its control actuators and instruments, a seamless circular projection with 240 degree viewing angle, a 5.1 multichannel audio system, as well as a unique five DOF motion system to guarantee full immersion of the driver in the virtual environment. Moreover, the acting accelerations and angular velocities are recorded using an Inertial Measurement Unit (IMU) that is installed close to the driver's head position in order to rate the quality of the applied Motion Cueing strategy. In the following, the basic hardware configuration and the dynamic motion system of this simulator will be discussed in detail, as they provide a general understanding of the underlying principles behind the control algorithms presented in Sections III and IV.

A. Simulator Hardware Configuration

To demonstrate its architecture and the interaction of all components within the interactive driving simulation, Figure 4 schematically sketches an overview of the implemented signal and information processing structure. The human driver inside the vehicle chassis, the so-called mockup, forms the core of this simulation setup. With the help of the generated Motion Cues, the driver evaluates the current driving state and performs his steering and pedal inputs to fulfill a specific driving task. Via CAN bus communication, these

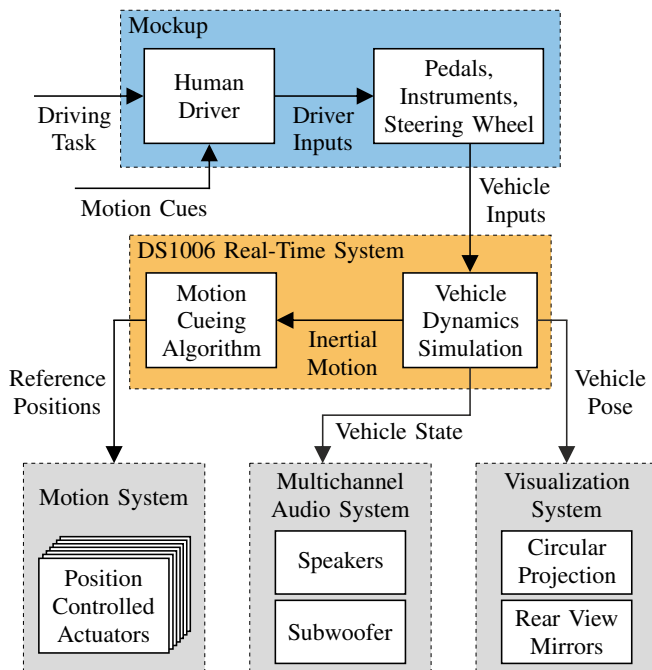


Figure 4. Overview of the Signal and Information Processing.

signals are subsequently processed by a dSPACE DS1006 real-time system using an AMD Opteron CPU @ 2.8GHz, where they serve as inputs for the simulated vehicle in the virtual environment. Here, the *Automotive Simulation Models* (ASM) tool suite is used as vehicle dynamics model, since it is a commercial multibody model that features all relevant subsystems of a real vehicle such as engine, powertrain, axle kinematics, as well as electronic control units and is therefore well-established in automotive applications [10]. The fixed sampling rate thereby is 1kHz, so that all virtual vehicle signals are available without significant latencies. In this way, the computed vehicle pose, consisting of its position and orientation, is determined every millisecond and transmitted to the visualization system. This pose is then displayed with a frequency of 60Hz on the circular projection, consisting of eight high definition projectors, and three rear view mirror monitors, giving the driver inside the simulator the impression of a fluid movement through the simulated environment. Further information on the applied rendering process of the virtual scenes using the game engine Unity3D is given in [2]. In addition, the characteristic soundscape of the simulated vehicle and other traffic participants is generated according to the calculated vehicle states, such as velocities and engine speeds for example, and reproduced via the installed audio system within the visualization dome. The inertial motion from the vehicle dynamics simulation, specifically the virtual vehicles accelerations and angular velocities, simultaneously serve as an input for the Motion Cueing Algorithm, which is also executed on the real-time system. As described before, the MCA determines suitable control signals for the dynamic motion system to generate the required vestibular stimuli within its physical limitations. In case of the ATMOS driving simulator these control signals contain the reference positions of seven position controlled servo asynchronous motors that drive the system. In the following, the components and the resulting kinematic relations are presented in detail to provide a deeper understanding of this unique motion system.

B. Dynamic Motion System

Different from conventional hexapods [11], the motion system of the ATMOS driving simulator is designed as a hybrid kinematics system, which is composed of two mechanically coupled components that can be actuated independently. To illustrate the functionality, Figure 5 shows an exploded view based on the multibody model of the system. The shaker system below the mockup is equipped with three crankshaft drives to perform vertical translational movements, as well as to rotate the driver around the roll and pitch axis. Thus, the shaker replicates the simulated vehicle movements relative to the road surface with exception of yaw motion and can further be used to increase the effect of the tilt coordination by expanding the rotational workspace of the motion system. In addition to the shaker, the motion platform performs movements in lateral and longitudinal direction via four actuated cross-undercarriages that are driven on V-shaped tracks. Because of these tilted tracks, each translational movement of the motion platform leads simultaneously to an additional rotation around the corresponding axes. As a direct consequence of these coupled kinematics, performing pure translational movements of the motion system is only possible within a very small range of the overall workspace, in which the forced rotations of the motion platform can be compensated using the shaker. However, it should be noted that this considerably restricts the shaker systems remaining workspace in its residual degrees of freedom.

To clarify the kinematic properties, the available workspace of the motion platform center point is illustrated in Figure 6. It can be seen that any translational movement causes besides a rotation of the motion platform also a vertical displacement of the center point due to the underlying kinematic constraints.

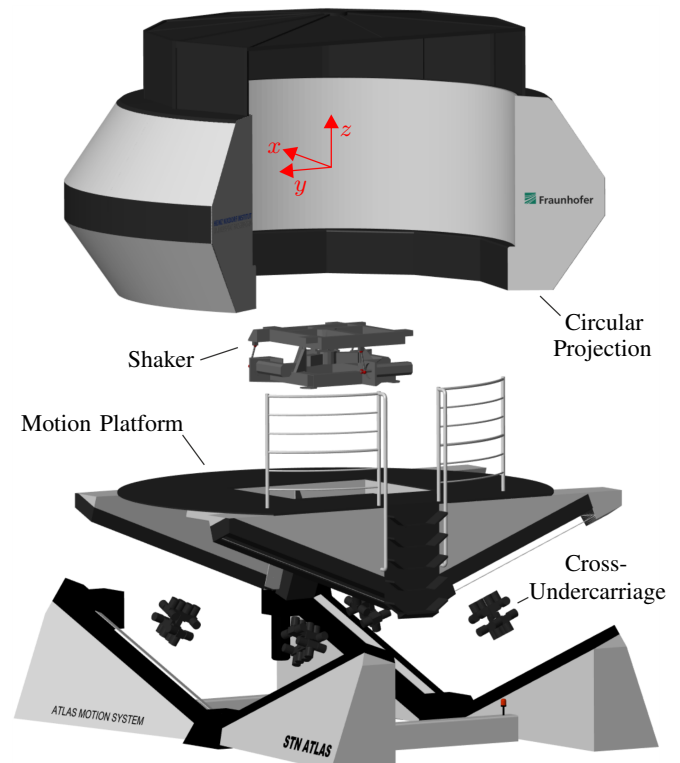


Figure 5. Exploded View of the Simulator Multibody Model.

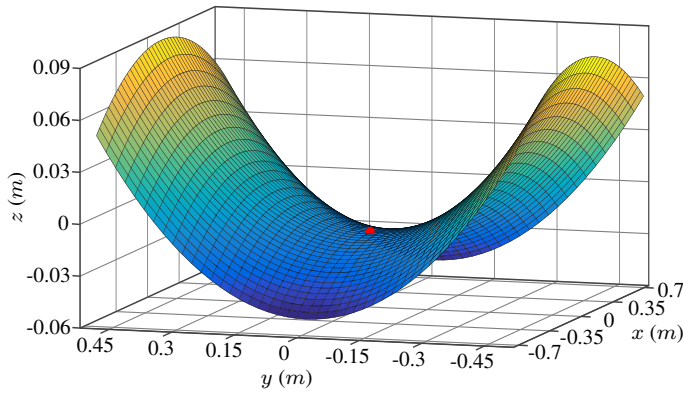


Figure 6. Workspace of the Motion Platform Center Point.

Thus, longitudinal movements always cause a lowering of the platform center, while lateral movements lift it. As a consequence, the motion platform performs movements along the curved surface shown in Figure 6, leading to an additional kinematic coupling between the translational DOF. Analogously, the analysis of the available shaker workspace leads to the dependencies between vertical displacements z , roll inclinations φ and pitch inclinations θ presented in Figure 7. As shown, a maximum vertical displacement of $z = \pm 72 \text{ mm}$ is feasible with the shaker. However, this is only practicable if there are no simultaneous tilts of the system, since additional roll and pitch angles not equal to zero considerably reduce the vertical workspace. Roll movements are generated by an alternating actuation of both front crankshaft drives, which are installed symmetrically to the roll axis. Thus, also a symmetric workspace results, as it is pictured top left in Figure 7. In contrast, pitch rotations are generated by actuating the two crankshaft drives in the front and the crankshaft drive in the rear in opposite directions. Due to the geometric properties of the system, the rear actuator reaches its top or bottom dead center at an angle of $\theta = \pm 5^\circ$. A tilt up to the maximum

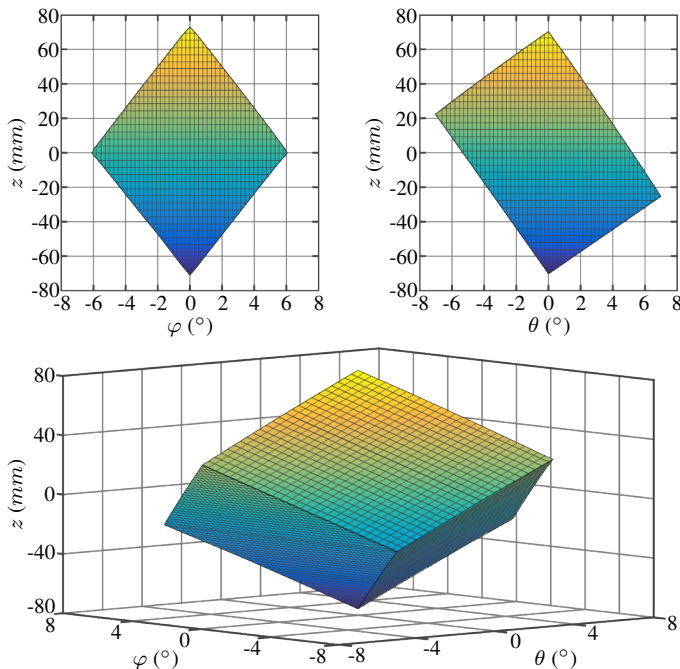


Figure 7. Analysis of the Shaker System Workspace.

pitch angle of $\theta = \pm 7^\circ$ is then possible by further movements of the front two actuators, but this simultaneously leads to a lifting or lowering of the shaker platform, as shown in the upper right corner of Figure 7. As a consequence, an asymmetrical workspace results. The combination of both upper graphics leads to the overall workspace of the shaker illustrated in the bottom of Figure 7. It shows that there are also interdependencies between the individual DOF of the shaker system, which can in the case of pitch rotations even cause undesired vertical movements of the driver in the simulator. Together with the nonlinear kinematic properties of the motion platform, these aspects has to be considered in the design of the Motion Cueing Algorithm in order to avoid conflicting sensory information, so-called *False Cues*, which typically lead to the undesired effect of *Simulator Sickness* for the driver [12].

Thus, due to the mentioned features of the ATMOS driving simulator, suitable control strategies are required since the implementation of the conventional CWA according to Figure 2 does not result in the desired quality of the motion rendering.

III. MODIFIED WASHOUT ALGORITHM

As described in Section I, the general idea of the Classical Washout Algorithm is based on an independent consideration of the systems degrees of freedom, which is due to the fact that the MCA was developed for application on a conventional hexapod. Because of this, the algorithm is not suitable for application on the ATMOS driving simulator introduced in the previous section, as there is a connection between translation and rotation because of the underlying kinematics of the motion system. For this reason, we subsequently present an extension of the classical approach that includes the relevant kinematic effects and enables a sufficient control quality. Moreover, a further analysis using system theoretical methods is described in [13].

A. Dynamic Position Washout

In case of the regarded driving simulator, each longitudinal and lateral movement of the motion platform generates a forced tilting around the corresponding roll and pitch axis. These rotations should ideally be used to emulate sustained accelerations using the tilt coordination technique. Otherwise, the tilt coordination has to be performed only by the shaker, which limits the maximum possible inclination to the small shaker workspace (see Figure 7). In contrast to the classical algorithm, a dynamic position washout is therefore required that enables the motion platform to drift into a defined end position within its workspace after it has performed the high-frequency movements. By determining this end position according to the associated inclination, low-frequency accelerations can also be simulated via the motion platform. For this purpose, the high-pass (hp) and washout (wo) filters of the high-frequency longitudinal and lateral acceleration paths are supplemented by further first order low-pass filters with variable gains K , as shown in Figure 8 using the example of longitudinal acceleration a_x . According to the shown structure, the corresponding transfer function G , that describes the dynamic behavior between the acceleration input a_x and the longitudinal simulator position x , is given as

$$G(s) = \frac{T_{hp}s + K}{T_{hp}s + 1} \cdot \frac{T_{wo}^2 s^2}{T_{wo}^2 s^2 + 2DT_{wo}s + 1} \cdot \frac{1}{s^2} \quad (1)$$

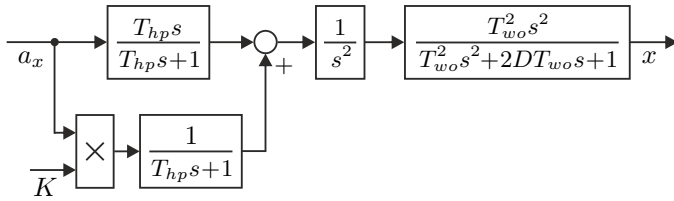


Figure 8. Extended Longitudinal High-Frequency Acceleration Path.

The non-intuitive idea of this extension can be clarified by the application of the final value theorem of the Laplace transform. Therefore, let a_x be a sustained acceleration input from the vehicle dynamics simulation, which can be assumed to be approximately constant, since the magnitude does not significantly change. For the integrated simulator position x follows then with increasing time $t \rightarrow \infty$:

$$\lim_{t \rightarrow \infty} x(t) = \lim_{s \rightarrow 0} s \cdot G(s) \cdot \underbrace{a_x}_{X(s)} = K \cdot T_{wo}^2 \cdot a_x \quad (2)$$

Consequently, the resulting simulator position depends on the gain K , the time constant T_{wo} of the washout filter as well as the amplitude of the acting acceleration a_x . If this position is now required to have a defined value x_{tc} , the necessary gain K can be determined corresponding to (2) as

$$K = \frac{x_{tc}}{T_{wo}^2 \cdot a_x} \quad (3)$$

Here, the singularity occurring for $a_x = 0 \text{ m/s}^2$ is not critical, since in this case the entire transfer function G is also multiplied with this input variable, resulting in a position $x = 0 \text{ m}$. The overall stability of the proposed structure is therefore always guaranteed as long as high-pass and washout filters possess a stable pole configuration, which is generally to be expected. Analogously, the initial value theorem of the Laplace transform can be used to show that the extension by the variable gain low-pass filter, as shown in Figure 8, does not negatively affect the reproduction of high-frequency acceleration components [13]. Like in the Classical Washout Algorithm, the dynamics of the drift into the end position x_{tc} can be specified by the parameters of the washout filter, which represents an important design freedom in the parameterization of the proposed control strategy.

The described extension is also implemented for the lateral high-frequency acceleration path, so that a washout in the defined position y_{tc} analogue to (3) is realized and thus sustained lateral stimuli are produced by a corresponding roll rotation of the motion platform.

B. Tilt Coordination Distribution

Due to the hybrid kinematics motion system, as well as the presented dynamic position washout, the tilt coordination technique can be performed either using the motion platform (mp), the shaker (sh) or a combination of both systems. The latter significantly increases the workspace and thus the maximum low-frequency acceleration amplitudes that can be generated. Consequently, a distribution strategy has to be specified, which enables a suitable coordination of both components. For this reason, an adaptation of the low-frequency longitudinal and lateral acceleration paths is conducted according to Figure 9. As shown with the example of the longitudinal acceleration,

a first order low-pass (lp) filter extracts the sustained acceleration components from the reference signal a_x , which are subsequently converted to the corresponding tilt coordination pitch angle θ_{tc} . In doing so, the associated rotation rate is limited to the well-established value of 0.1 rad/s , in order that the tilt coordination technique does not disturb the driving impression of the human driver [14]. In contrast to conventional hexapods, this inclination is divided among the subsystems of the motion system by introducing a distribution coefficient $\alpha \in \mathbb{R}$ with $0 \leq \alpha \leq 1$. This results in the inclinations for the shaker θ_{sh} and for the motion platform θ_{mp} that are necessary to replicate the low-frequency accelerations by the gravitational force. Based on the known kinematic relations of the motion platform, an equivalent platform position x_{tc} , which corresponds to the required inclination, is subsequently determined. This position equivalent then serves as input for calculating the variable gain K according to (3) so that the coupling between translational and rotational DOF is taken into account. Equally, this process is implemented for the lateral low-frequency acceleration path.

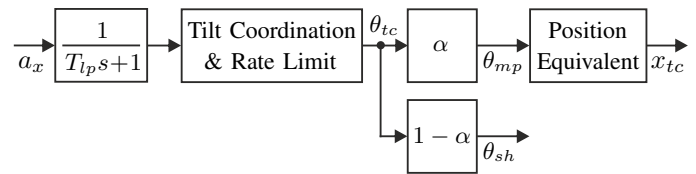


Figure 9. Extended Longitudinal Low-Frequency Acceleration Path.

C. Resulting Algorithm Structure and Parameterization

The combination of dynamic position washout and tilt coordination distribution leads to the overall structure of the modified washout algorithm illustrated in Figure 10. Based on the principles of the Classical Washout Algorithm, this filter-based control strategy enables the generation of suitable control signals in the form of position and orientation commands for the motion system of the ATMOS driving simulator. Using the inverse kinematics of the motion platform and the shaker, the required reference angles of the position controlled actuators are determined, enabling the motion system to generate the vestibular Motion Cues according to the current driving situation. In order to ensure that these references are adjusted to the system with a desired dynamic behavior, a model-based approach to compensate existing actuator latencies is presented in [13]. The estimation of the associated filter parameters and distribution coefficients was performed by numerical optimization using a defined driving maneuver. Here, the rural road drive, which will be introduced in one of the next sections, was chosen since it represents a good compromise between moderate driving scenarios and extreme maneuvers at the limits of driving dynamics. Table I provides an overview of the resulting parameters.

Although the developed algorithm is motivated by the specific features of the motion system, in particular the concept of a dynamic position washout offers great potential to transfer and combine it with alternative Motion Cueing approaches. For example, an integration of the approach into predictive algorithms is possible in order to use information of the current vehicle state and the oncoming road conditions to preposition the motion system. Thus, the available simulator

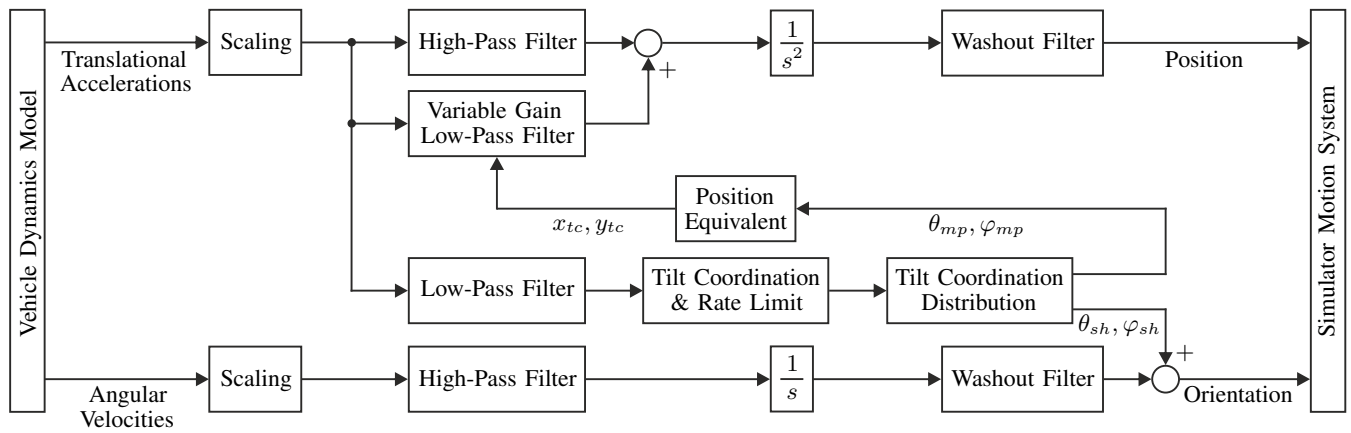


Figure 10. Overall Structure of the Developed Washout Algorithm.

TABLE I. APPLIED ALGORITHM PARAMETERS.

Scaling	1st Order HP Filter	1st Order LP Filter	2nd Order WO Filter	Distribution Coefficient
$k_x = 0.4$	$T_{hp} = 0.95$	$T_{lp} = 0.95$	$T_{wo} = 0.49,$ $D = 0.7$	$\alpha_x = 0.65$
$k_y = 0.4$	$T_{hp} = 0.6$	$T_{lp} = 0.6$	$T_{wo} = 0.44,$ $D = 1.0$	$\alpha_y = 0.6$
$k_z = 1.0$	$T_{hp} = 0.4$	-	$T_{wo} = 0.45,$ $D = 1.0$	-
Scaling	1st Order HP Filter	1st Order LP Filter	1st Order WO Filter	Distribution Coefficient
$k_\varphi = 1.0$	$T_{hp} = 1.2$	-	$T_{wo} = 0.8$	-
$k_\theta = 1.0$	$T_{hp} = 0.3$	-	$T_{wo} = 0.2$	-

workspace is used more efficiently [15]. For this purpose, suitable positions are determined at runtime instead of x_{tc} and y_{tc} , to which the motion system drifts after executing the high-frequency movements. Occurring false cues caused by the dynamic position washout can thereby be masked by the gravitational force using an additional tilt of the driving simulator [9].

IV. MODEL PREDICTIVE CONTROL APPROACH

While the presented modified washout algorithm takes into account coupling effects between translational and rotational DOF of the ATMOS driving simulator, this filter-based control strategy does not consider interdependencies between the particular translational movements. That can be explained by the underlying algorithm structure, which is basically comparable to the CWA with its independent treatment of all system degrees of freedom. To overcome this, an optimization-based Motion Cueing Algorithm using the concept of Model Predictive Control was introduced in [16]. It offers the advantage that hard constraints, such as the workspace limitations and kinematic relations described in Section II, can be explicitly integrated into a numerical optimization process, which is performed at runtime. Furthermore, by including an actuator dynamics model it is ensured that the determined motion trajectory is always feasible for the driving simulator. In the following, the main aspects of the MPC-based algorithm are explained in detail to provide a basic understanding for the comparison of both control approaches in the next section.

A. Nonlinear Motion System Model

According to the basic idea of the established MPC paradigm, a constrained optimal control problem is numeri-

cally solved over a receding time horizon at each calculation cycle. Subsequently, only the first element of the computed trajectory is applied to the process and the procedure is iterated [17]. Thereby, the resulting control quality depends significantly on the availability of an adequate process model to predict the future system behavior. This model consequently has to cover all relevant dynamic and kinematic effects on the one hand. At the same time an online optimization causes a significant computational effort, for which reason the integrated system model must be designed as simple as possible to meet the real-time requirements.

Driving simulators are large-scale systems with high inertia, so there is always a specific dynamic behavior, which influences the control quality and therefore has to be considered in the planning of the simulator motion trajectory. Assuming that the basic mechanical system is a rigid body without significant elasticities, the overall system dynamics can be expressed by the transfer behavior of the installed actuators. In case of the considered motion system, the input/output dynamics of each position controlled actuator is described by a linear third order lag element with the state space representation

$$\begin{aligned}\dot{x}_s(t) &= A_s \cdot x_s(t) + B_s \cdot u_s(t) \\ y_s(t) &= C_s \cdot x_s(t).\end{aligned}\quad (4)$$

Here, the associated state vector $x_s(t) \in \mathbb{R}^3$ contains the angle $\psi(t)$ of a servo motor, its angular velocity $\dot{\psi}(t)$ and its angular acceleration $\ddot{\psi}(t)$:

$$x_s(t) = [\psi(t) \quad \dot{\psi}(t) \quad \ddot{\psi}(t)]^T \quad (5)$$

The input and output variables of the model from (4) form the reference position $\psi_{ref}(t)$ determined from the MCA and the actual angle $\psi(t)$ of the controlled actuator:

$$\begin{aligned}u_s(t) &= \psi_{ref}(t) \\ y_s(t) &= \psi(t)\end{aligned}\quad (6)$$

Consequently, the state differential equation matrices result as

$$A_s = \begin{bmatrix} 0 & 1 & 0 \\ 0 & 0 & 1 \\ -a_0 & -a_1 & -a_2 \end{bmatrix} \in \mathbb{R}^{3 \times 3}, \quad B_s = \begin{bmatrix} 0 \\ 0 \\ b_0 \end{bmatrix} \in \mathbb{R}^3, \quad (7)$$

so that a time-invariant *Single-Input-Single-Output* (SISO) system in controllable canonical form is given for each controlled actuator. As already explained in Section II, the motion system

of the ATMOS driving simulator is equipped with a total number of seven servo motors. Three of these are used to actuate the shaker, while two identical servo motors, which are controlled with the same reference positions $\psi_{ref}(t)$, each drive the motion platform in longitudinal and lateral direction. Therefore, in the derived simulator model, the four actuators of the motion platform can be combined to one actuator per longitudinal and lateral DOF to reduce the resulting model complexity. Summarizing all five actuator models finally leads to a 15th order linear system with the state differential equation

$$\dot{x}(t) = A \cdot x(t) + B \cdot u(t). \quad (8)$$

Since the underlying position controllers are very exact and the actuators can thus be assumed to be completely decoupled, the state matrix $A \in \mathbb{R}^{15 \times 15}$ and the input matrix $B \in \mathbb{R}^{15 \times 5}$ are block diagonal matrices that contain the state differential equations according to (4) of all five servo motors on their main diagonals. The corresponding state vector $x(t) \in \mathbb{R}^{15}$ results from the state variables of each actuator given in (5), while the input vector $u(t) \in \mathbb{R}^5$ is a vector obtained from the respective reference positions $\psi_{ref}(t)$.

In order to respect the relevant kinematic characteristics of the simulator explicitly in the control algorithm, a functional relationship between the state variables of (8) and the control variables, more precisely the acting translational accelerations $a(t)$ and angular velocities $\omega(t)$, is required. Moreover, these output quantities need to be described at the driver's head position since the vestibular perception organs are located in the human inner ear [18].

For this purpose, the direct kinematics of the motion system are defined in Cartesian coordinates as

$$\begin{aligned} {}^I r_h(\psi(t)) &= {}^I r_{mp}(\psi(t)) + {}^I r_{sh}(\psi(t)) \\ {}^I \beta_h(\psi(t)) &= {}^I \beta_{mp}(\psi(t)) + {}^I \beta_{sh}(\psi(t)) \end{aligned} \quad (9)$$

in the first instance. According to Figure 11, the pose of the driver's head position h is given by the position and orientation vectors ${}^I r_h = {}^I [x \ y \ z]^T \in \mathbb{R}^3$ and ${}^I \beta_h = {}^I [\varphi \ \theta]^T \in \mathbb{R}^2$ in the inertial reference frame I . These are expressed as functions of all five actuator angles $\psi(t)$, which form the systems generalized coordinates in that context. Because the

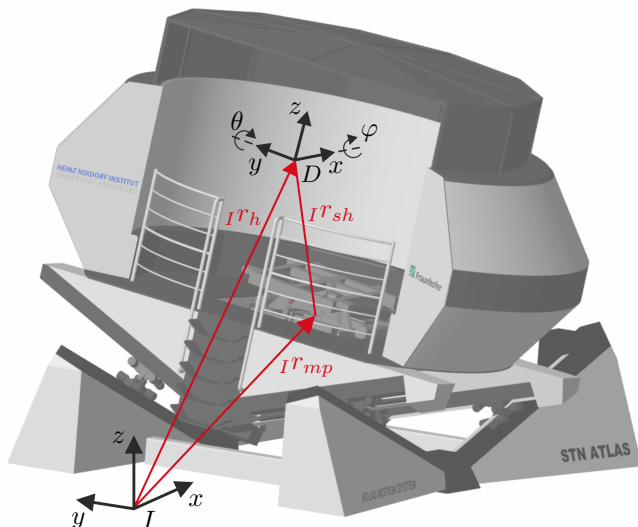


Figure 11. Scheme of the Driver's Head Position Pose.

mechanical coupling between the motion platform and the shaker represents a serial kinematics, the positions and orientations of both subsystems are added as shown in (9). To obtain the associated translational and angular velocities, the time derivatives of both vectors are determined:

$$\begin{aligned} {}^I v_h(\psi(t), \dot{\psi}(t)) &= \frac{d {}^I r_h(\psi(t))}{dt} = \frac{\partial {}^I r_h(\psi(t))}{\partial \psi(t)} \cdot \dot{\psi}(t) \\ {}^I \dot{\beta}_h(\psi(t), \dot{\psi}(t)) &= \frac{d {}^I \beta_h(\psi(t))}{dt} = \frac{\partial {}^I \beta_h(\psi(t))}{\partial \psi(t)} \cdot \dot{\psi}(t) \end{aligned} \quad (10)$$

Hence, the velocity variables of the driver's head position are calculated from the product of the actuator angular velocities $\dot{\psi}(t)$ and the partial derivatives of (9) to the generalized coordinates $\psi(t)$, which is known as the *Jacobian matrix*. A further differentiation of the velocity vector ${}^I v_h(t)$ then yields the desired expression of the translational accelerations ${}^I a_h = {}^I [\ddot{x} \ \ddot{y} \ \ddot{z}]^T$ according to

$$\begin{aligned} {}^I a_h(\psi(t), \dot{\psi}(t), \ddot{\psi}(t)) &= \frac{d {}^I v_h(\psi(t), \dot{\psi}(t))}{dt} \\ &= \frac{\partial^2 {}^I r_h(\psi(t))}{\partial \psi(t)^2} \cdot \dot{\psi}^2(t) + \frac{\partial {}^I r_h(\psi(t))}{\partial \psi(t)} \cdot \ddot{\psi}(t). \end{aligned} \quad (11)$$

As shown, besides the state variables of (8) and the Jacobian matrix, also the second partial derivatives of the position vector ${}^I r_h(t)$ to the actuator angles $\psi(t)$ are required to determine the acting accelerations at the driver's head position. In addition, the angular velocity vector ${}^I \omega_h(t)$ is obtained from the derivatives of the orientations ${}^I \beta_h(t)$ according to (10) as

$${}^I \omega_h(\psi(t), \dot{\psi}(t)) = \begin{bmatrix} \cos \theta & 0 \\ 0 & 1 \end{bmatrix} \cdot {}^I \begin{bmatrix} \dot{\varphi}(\psi(t), \dot{\psi}(t)) \\ \dot{\theta}(\psi(t), \dot{\psi}(t)) \end{bmatrix}. \quad (12)$$

As it is a basic principle of rigid body mechanics, this relation is not further discussed at this point.

In order to consider the current orientation of the motion system in the optimization process, the translational accelerations ${}^I a_h(t)$ and angular velocities ${}^I \omega_h(t)$ are transformed into the fixed reference system D of the driver, which is assumed to be orientated identically to the shaker reference frame (see Figure 11):

$$\begin{aligned} {}^D a_h(\psi(t), \dot{\psi}(t), \ddot{\psi}(t)) &= L_{DI} \cdot {}^I a_h(\psi(t), \dot{\psi}(t), \ddot{\psi}(t)) \\ {}^D \omega_h(\psi(t), \dot{\psi}(t)) &= T_{DI} \cdot {}^I \omega_h(\psi(t), \dot{\psi}(t)) \end{aligned} \quad (13)$$

using the rotation matrices

$$\begin{aligned} L_{DI} &= \begin{bmatrix} \cos \theta & 0 & -\sin \theta \\ \sin \varphi \cdot \sin \theta & \cos \varphi & \sin \varphi \cdot \cos \theta \\ \cos \varphi \cdot \sin \theta & -\sin \varphi & \cos \varphi \cdot \cos \theta \end{bmatrix}, \\ T_{DI} &= \begin{bmatrix} \cos \theta & 0 \\ \sin \varphi \cdot \sin \theta & \cos \varphi \end{bmatrix} \end{aligned} \quad (14)$$

At this point it becomes clear that the matrices of (12) and (14) differ from the formulations reported in literature, which is due to the fact that the ATMOS driving simulator cannot perform any rotations around the vertical axis. Consequently, the yaw angle is not taken into account, while the roll and pitch angles $\varphi(t)$ and $\theta(t)$ are determined according to (9) as functions of the state variables $\psi(t)$.

Since the low-frequency components of the longitudinal and lateral acceleration reference from the simulated vehicle cannot be replicated by translational displacements of the

motion system because of its limited workspace, the previously described tilt coordination technique is applied. For this purpose, the gravitational acceleration vector g is transformed into the fixed coordinate system of the driver by means of the rotation matrix L_{DI} as

$${}_D g = L_{DI} \cdot \begin{bmatrix} 0 \\ 0 \\ -g \end{bmatrix} = {}_D \begin{bmatrix} g \cdot \sin \theta(t) \\ -g \cdot \sin \varphi(t) \cdot \cos \theta(t) \\ -g \cdot \cos \varphi(t) \cdot \cos \theta(t) \end{bmatrix}. \quad (15)$$

By combining the transformed translational accelerations of (13) with the gravitational acceleration vector ${}_D g$ from the tilt coordination, the so-called *specific accelerations* $a(t) = {}_D a_h(t) - {}_D g(t)$ are obtained, which are commonly used in Motion Cueing applications:

$$a(t) = \begin{bmatrix} \ddot{x}(t) \\ \ddot{y}(t) \\ \ddot{z}(t) \end{bmatrix}_h - {}_D \begin{bmatrix} g \cdot \sin \theta(t) \\ -g \cdot \sin \varphi(t) \cdot \cos \theta(t) \\ -g \cdot \cos \varphi(t) \cdot \cos \theta(t) \end{bmatrix} \quad (16)$$

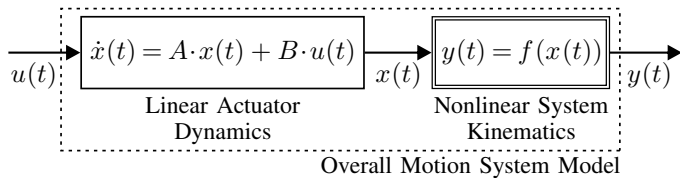
A condensed overview of the resulting process model to predict the future motion system behavior is given in Figure 12. As illustrated, it features the typical structure of a *Wiener model*, consisting of a series connection of a linear dynamic system in front of a static nonlinearity [19]. The overall system description thus is given in the form of the nonlinear state space representation

$$\begin{aligned} \dot{x}(t) &= A \cdot x(t) + B \cdot u(t) \\ y(t) &= f(x(t)). \end{aligned} \quad (17)$$

Here, the linear state differential equation describes the dynamic transfer behavior of all controlled actuators analogously to (8). In addition, the output equation contains the kinematic relations derived in (9)–(16), summarized in the generalized vector function f , to determine the desired output variables $y(t)$ at the driver's head position within the simulator. By using the proposed model of (17), all relevant characteristics of the motion system described in Section II, such as physical limitations of the available workspace and coupling effects between individual DOF, are explicitly considered in the control algorithm, which represents one of the key features of the developed optimization-based MCA. However, the integration of all kinematic dependencies causes a significant computational effort due to the underlying model complexity. The following section therefore presents a method for efficiently calculating the future system behavior as a function of the control variables $\psi_{ref}(t)$.

B. Prediction of the Future System Behavior

In order to plan the motion trajectory of the simulator adequately for the oncoming driving situation, the future



where

$$x(t) = \begin{bmatrix} \psi(t) \\ \dot{\psi}(t) \\ \ddot{\psi}(t) \end{bmatrix} \in \mathbb{R}^{15}, \quad y(t) = {}_D \begin{bmatrix} a(t) \\ \omega(t) \end{bmatrix} \in \mathbb{R}^5, \quad u(t) = \psi_{ref}(t) \in \mathbb{R}^5$$

Figure 12. Resulting Nonlinear Motion System Model.

system behavior has to be specified within a limited time horizon, the so-called *prediction horizon* N , with respect to the actuating variables. This prediction is usually performed using a discrete system description, since the application of a time-continuous process model is more complex without providing any considerable benefits [20].

For this reason, the solution of the state differential equation of (17) is determined using the *state-transition matrix*. According to [21] follows thus:

$$\begin{aligned} x(k+1) &= e^{A \cdot T} \cdot x(k) + \int_0^T e^{A \cdot (T-\tau)} \cdot B \cdot u(k) \, d\tau \\ &= e^{A \cdot T} \cdot x(k) + \int_0^T e^{A \cdot (T-\tau)} \, d\tau \cdot B \cdot u(k) \end{aligned} \quad (18)$$

This assumes that the value of the input vector $u(k)$ does not change within the duration T of a discrete time step k , and therefore does not have to be considered within the integral. The solution of (18) then yields

$$x(k+1) = e^{A \cdot T} \cdot x(k) + A^{-1} \cdot (e^{A \cdot T} - I) \cdot B \cdot u(k). \quad (19)$$

Here, A is required to be a nonsingular matrix, so that its inverse A^{-1} exists. For the given application, however, it can be assumed that the underlying position controls of the actuators are stable and A hence has no eigenvalues equal to zero, for which reason this condition is fulfilled here. In the following, (19) is rewritten in the more compact notation

$$x(k+1) = A_d \cdot x(k) + B_d \cdot u(k), \quad (20)$$

with the corresponding matrices

$$\begin{aligned} A_d &= e^{A \cdot T} \\ B_d &= A^{-1} \cdot (e^{A \cdot T} - I) \cdot B. \end{aligned} \quad (21)$$

Consequently, the time-discrete form of the state space representation (17) finally results as

$$\begin{aligned} x(k+1) &= A_d \cdot x(k) + B_d \cdot u(k) \\ y(k) &= f(x(k)). \end{aligned} \quad (22)$$

From this, the future state variables $x(k+1) \dots x(k+N)$ within the prediction horizon N are determined according to

$$\begin{aligned} x(k+1) &= A_d \cdot x(k) + B_d \cdot u(k) \\ x(k+2) &= A_d \cdot x(k+1) + B_d \cdot u(k+1) \\ &= A_d^2 \cdot x(k) + A_d \cdot B_d \cdot u(k) + B_d \cdot u(k+1) \\ &\vdots \\ x(k+N) &= A_d^N \cdot x(k) + A_d^{N-1} \cdot B_d \cdot u(k) + \dots + \\ &\quad A_d \cdot B_d \cdot u(k+N-2) + B_d \cdot u(k+N-1) \end{aligned} \quad (23)$$

by multiplying the system matrices A_d and B_d . For the further proceeding it is recommended to formulate these expressions as a vector equation of the form:

$$\bar{x}(k+1) = F \cdot x(k) + G \cdot \bar{u}(k) \quad (24)$$

where

$$\bar{x}(k+1) = \begin{bmatrix} x(k+1) \\ x(k+2) \\ \vdots \\ x(k+N) \end{bmatrix} \in \mathbb{R}^{15 \cdot N}, \quad F = \begin{bmatrix} A_d \\ A_d^2 \\ \vdots \\ A_d^N \end{bmatrix} \in \mathbb{R}^{15 \cdot N \times 15},$$

$$G = \begin{bmatrix} B_d & 0 & \dots & 0 \\ A_d B_d & B_d & \dots & 0 \\ \vdots & \vdots & \ddots & \vdots \\ A_d^{N-1} B_d & A_d^{N-2} B_d & \dots & B_d \end{bmatrix} \in \mathbb{R}^{15 \cdot N \times 5 \cdot N},$$

$$\bar{u}(k) = \begin{bmatrix} u(k) \\ u(k+1) \\ \vdots \\ u(k+N-1) \end{bmatrix} \in \mathbb{R}^{5 \cdot N} \quad (25)$$

Thus, the future state variables depend on the actual system state $x(k)$, which is known by measurement and observation, as well as the optimization variables $u(k) \dots u(k+N-1)$. Moreover, since the transfer behavior of the controlled actuators is time-invariant, the prediction matrices of (25) can already be calculated offline during the initialization process of the controller, which improves compliance with the real-time capability. In contrast, the prediction of the corresponding output variables $y(k+i) \forall i = 1 \dots N$, causes a large numerical effort, as these include the direct kinematic relations of the motion system. That is why an approximation of the nonlinearities of (22) within the prediction horizon is pursued in each calculation cycle, leading to a significant reduction of the computational load. Specifically, a first order *Taylor series* of the nonlinear output equation is determined as

$$y(k+i) \approx f(x(k)) + \left. \frac{\partial f(x(k))}{\partial x} \right|_{x(k)} \cdot (x(k+i) - x(k)), \quad (26)$$

where the partial derivative of the vector function f to the state vector with the value $x(k)$ yield the linear output matrix $C(k) \in \mathbb{R}^{5 \times 15}$. By rearranging (26), a more structured formulation is obtained:

$$y(k+i) \approx C(k) \cdot x(k+i) + \underbrace{f(x(k)) - C(k) \cdot x(k)}_{h(k)} \quad (27)$$

Consequently, the linear affine output equation (27) results in each calculation cycle of the optimization-based controller, which approximates the nonlinear system behavior within the considered prediction horizon. Depending on the selected sampling rate, a high-frequency update of the output matrix $C(k)$ thus is performed, based on the feedback state vector $x(k)$. Furthermore, the term $h(k)$ is obtained, which depends only on the current system information and is therefore constant in the prediction range $i = 1 \dots N$. As this is usually limited to only a few seconds [22], the approximation of (27) provides a sufficiently accurate description of all relevant kinematic effects to optimize the simulator motion trajectory.

Although $C(k)$ and $h(k)$ must first be calculated at the beginning of each prediction sequence, the future output variables $y(k+i)$ can then be determined very efficiently according to

$$\begin{aligned} y(k+1) &= C(k) \cdot x(k+1) + h(k) \\ y(k+2) &= C(k) \cdot x(k+2) + h(k) \\ &\vdots \\ y(k+N) &= C(k) \cdot x(k+N) + h(k). \end{aligned} \quad (28)$$

Together with the state variable prediction specified in (24), this yields the future outputs in vector notation:

$$\begin{aligned} \bar{y}(k+1) &= C \cdot \bar{x}(k+1) + H \\ &= C \cdot F \cdot x(k) + C \cdot G \cdot \bar{u}(k) + H \end{aligned} \quad (29)$$

where

$$\bar{y}(k+1) = \begin{bmatrix} y(k+1) \\ y(k+2) \\ \vdots \\ y(k+N) \end{bmatrix} \in \mathbb{R}^{5 \cdot N}, \quad H = \begin{bmatrix} h(k) \\ h(k) \\ \vdots \\ h(k) \end{bmatrix} \in \mathbb{R}^{5 \cdot N},$$

$$C = \begin{bmatrix} C(k) & 0 & \dots & 0 \\ 0 & C(k) & \dots & 0 \\ \vdots & \vdots & \ddots & \vdots \\ 0 & 0 & \dots & C(k) \end{bmatrix} \in \mathbb{R}^{5 \cdot N \times 15 \cdot N} \quad (30)$$

As a result, (29) offers the advantage that only its first two summands have to be evaluated at runtime by simple matrix multiplications, instead of evaluating the nonlinear output equation of (22) for each single time step $k+i$ within the prediction horizon $i = 1 \dots N$.

C. Solution of the Optimal Control Problem

In order to reproduce the vestibular Motion Cues of the simulated vehicle, given by its translational accelerations and angular velocities, the optimal control problem

$$\begin{aligned} \text{minimize}_{\Delta \bar{u}(k)} & \sum_{i=1}^N \|y(k+i) - r(k+i)\|_Q^2 + \sum_{i=1}^N \rho(k+i) \\ & + \sum_{i=0}^{N-1} \|\Delta u(k+i)\|_R^2 + \|u(k+N-1)\|_S^2 \end{aligned} \quad (31)$$

subject to

$$\begin{aligned} x_{lo} &\leq x(k+i) \leq x_{up}, \quad i \in [1, N] \\ u_{lo} &\leq u(k+i) \leq u_{up}, \quad i \in [0, N-1] \end{aligned}$$

is solved numerically in each calculation cycle of the MPC-based algorithm. Here, the first and third summand of the cost function evaluate the control deviation as well as the change rate of the actuating variables $\Delta u(k) \dots \Delta u(k+N-1)$ for all time steps in prediction horizon, using the positive definite weighting matrices $Q \in \mathbb{R}^{5 \times 5}$ and $R \in \mathbb{R}^{5 \times 5}$. The control deviation results from the difference between the future output variables, which are expressed according to (29) as a function of the feedback state vector $x(k)$ and the optimization variables, and the simulated vehicle accelerations and angular velocities summarized in the reference vector

$$r(k+i) = \begin{bmatrix} a_{ref}(k+i) \\ \omega_{ref}(k+i) \end{bmatrix} \in \mathbb{R}^5 \quad \forall i = 1 \dots N. \quad (32)$$

However, since these references depend on the future driver inputs in the prediction horizon, they are generally not exactly known in the current time step k . It is therefore common practice to consider the vehicle references constant at each future time step, although this does not fully exploit the potential of the predictive controller [23]. To overcome this, we proposed a novel model-based online prediction strategy in [24]. As key features, this approach includes a simplified vehicle model as well as a virtual driver model based on established algorithms from nonlinear control theory to estimate future driver inputs

and the resulting vehicle reactions depending on the current driving situation and given route information. By means of measurement data from a real test drive, it was proven that the reproduced Motion Cues differ only slightly from those of an exactly known reference trajectory, which demonstrates the effectiveness of the developed approach. In the context of this paper, however, an a-priori known future reference is assumed, since the general functionality of the predictive MCA and its handling of the considered motion systems kinematic properties are to be highlighted.

In addition, the second summand of (31) denotes a *penalty term* to prevent deviations between the angular velocities of the reference signal and those of the motion system above a defined boundary. This enables the tilt coordination rotation rate as well as the forced rotations due to the kinematic couplings of the motion platform to be limited to a desired value ε , for example the perception threshold of the human vestibular organs:

$$\rho(k+i) = e^{\sigma \cdot (|\omega(k+i) - \omega_{ref}(k+i)| - \varepsilon)} \quad (33)$$

Selecting appropriate penalty weights $\sigma \gg 1$, the limitation of the rotation rate is taken into account in the numerical optimization, since the penalty term applies:

$$\rho(k+i) \begin{cases} \ll 1 & \text{if } |\omega(k+i) - \omega_{ref}(k+i)| < \varepsilon \\ = 1 & \text{if } |\omega(k+i) - \omega_{ref}(k+i)| = \varepsilon \\ \gg 1 & \text{if } |\omega(k+i) - \omega_{ref}(k+i)| > \varepsilon \end{cases} \quad (34)$$

Furthermore, the last element of the cost function represents a terminal cost to create a washout effect and return the simulator to its initial position. Here, the positive definite weighting matrix $S \in \mathbb{R}^{5 \times 5}$ determines the intensity of the washout movement. To comply with the physical limitations of the motion system, constraints on the state and actuating variables are included in (31). For this, lower and upper boundaries $(\cdot)_{lo}$ and $(\cdot)_{up}$ are defined according to the installed actuators performances and the available workspace.

The resulting optimal control problem is solved at runtime on the dSPACE DS1006 system with a sampling time of 25 ms, using the *conservative convex separable approximation* (CCSA) algorithm [25], which is provided by the *NLopt* open-source library for nonlinear optimization [26]. Thereby, the prediction horizon is chosen to $N = 40$ discrete time steps to realize a receding time horizon of one second. The constrained optimal control problem of (31) hence involves

200 optimization variables $\Delta \bar{u}(k)$ that are determined in real-time by the proposed control strategy. Figure 13 schematically shows the overall signal processing structure in a block diagram. In addition to the previously described methodology, it includes a state observer [27], enabling the complete state vector $x(k)$ to be determined in each time step k from the measured angular positions $\psi(k)$ and velocities $\dot{\psi}(k)$. The basis of this observer are the dynamic models of the controlled actuators according to (4).

V. COMPARISON OF THE CONTROL STRATEGIES

Since the scientific objective of this paper deals with the comparison of the filter- and optimization-based control algorithms presented in Sections III and IV, the underlying evaluation framework is described in detail at this point. The applied quality criteria are initially discussed for this purpose. Afterwards, the driving scenarios examined in this study will be briefly introduced.

A. Objective Quality Criteria

In order to compare both Motion Cueing strategies on the basis of an objective valuation metric, suitable quality criteria must be specified. Therefore, according to [28] and [29], we introduce performance indicators λ_1 and λ_2 that are defined as

$$\lambda_1 = \frac{1}{M} \sum_{j=0}^M \sqrt{\left(\frac{e_{a_x,j}}{a_{x,norm}}\right)^2 + \left(\frac{e_{a_y,j}}{a_{y,norm}}\right)^2 + \left(\frac{e_{a_z,j}}{a_{z,norm}}\right)^2} + \frac{1}{M} \sum_{j=0}^M \sqrt{\left(\frac{e_{\omega_x,j}}{\omega_{x,norm}}\right)^2 + \left(\frac{e_{\omega_y,j}}{\omega_{y,norm}}\right)^2} \quad (35)$$

and

$$\lambda_2 = \frac{1}{M} \sum_{j=0}^M \sqrt{\left(\frac{e_{\hat{a}_x,j}}{a_{x,norm}}\right)^2 + \left(\frac{e_{\hat{a}_y,j}}{a_{y,norm}}\right)^2 + \left(\frac{e_{\hat{a}_z,j}}{a_{z,norm}}\right)^2} + \frac{1}{M} \sum_{j=0}^M \sqrt{\left(\frac{e_{\hat{\omega}_x,j}}{\omega_{x,norm}}\right)^2 + \left(\frac{e_{\hat{\omega}_y,j}}{\omega_{y,norm}}\right)^2} \quad (36)$$

with

$$\begin{aligned} e_{a_i} &= a_{i,Ref} - a_i|_{i=x,y,z} \quad \text{and} \quad e_{\omega_i} = \omega_{i,Ref} - \omega_i|_{i=x,y} \\ e_{\hat{a}_i} &= \hat{a}_{i,Ref} - \hat{a}_i|_{i=x,y,z} \quad \text{and} \quad e_{\hat{\omega}_i} = \hat{\omega}_{i,Ref} - \hat{\omega}_i|_{i=x,y}. \end{aligned} \quad (37)$$

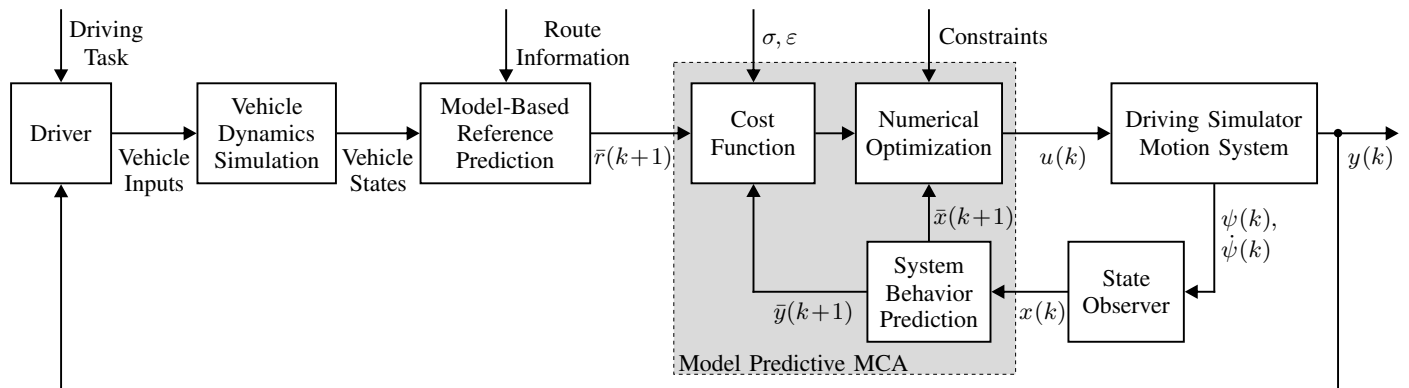


Figure 13. Signal Processing Structure of the MPC-Based Motion Cueing Strategy.

Here, (35) provides a measure of the physical deviations between the scaled reference accelerations $a_{i,Ref}$ and angular velocities $\omega_{i,Ref}$ from the vehicle dynamics simulation and the measured quantities in the driving simulator for the considered DOF. λ_1 therefore returns the averaged normalized control error over the number of measured values M within the considered time range. The normalization is necessary to obtain dimensionless quantities that allow a simultaneous consideration of accelerations and angular velocities on a common scale. According to [30], the human perception thresholds for movements are used as corresponding normalization factors $a_{i,norm}$ and $\omega_{i,norm}$. In addition, the indicator λ_2 as defined by (36) yields a measure for the perceived control quality, which can differ from the physical deviations due to the frequency-dependent dynamic behavior of the human vestibular organs, as well as perception thresholds. This causes, for example, that control errors in detectable frequency ranges are perceived more disturbing than deviations in undetectable ranges. To take these effects into account, well-established models of the human vestibular system illustrated in Figure 14 are included. Here, the primary perceptual organs are the semicircular canals, which enable the detection of angular velocities in all three rotational DOF, and the otoliths that are responsible for the perception of longitudinal, lateral and vertical accelerations.

According to Figure 15, the corresponding dynamic behavior is typically described by mechanical analogous models of the respective organs, which lead to the illustrated transfer functions with the inputs a_i and ω_i [32][33], as they are widely used in driving simulation applications [14]. In agreement with [34], the parameters of the otoliths model are selected to $K_{oto} = 0.4$, $T_1 = 5s$, $T_2 = 0.016s$ and $T_L = 10s$, while the semicircular canal model parameters are $K_{scc} = 5.73$, $T_1 = 5.73s$, $T_2 = 0.005s$, $T_L = 0.06s$ and $T_a = 80s$. This leads to the resulting frequency responses of the transfer functions $G_{oto}(j\omega)$ and $G_{scc}(j\omega)$ shown in Figure 16. It becomes clear that the semicircular canals serve as good angular velocity sensors in the frequency range from 0.05 to 3 Hz, since rotary motions are closely detected without amplitude changes and with only small phase shifts. This frequency spectrum is also characteristic for everyday driving maneuvers in traffic, which is why rotary vehicle movements can be easily perceived by the human vestibular apparatus. In contrast, low-frequency rotations are perceived strongly damped and are almost completely suppressed in case of a constant angular velocity. These characteristics of the semicircular canals are used in interactive driving simulation to apply the previously described tilt coordination technique without the driver being able to detect the unnatural rotational movements. In addition, the modeled otoliths show a frequency-specific

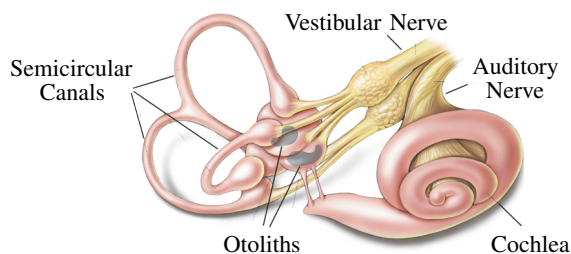


Figure 14. Vestibular System in the Human Inner Ear [31].

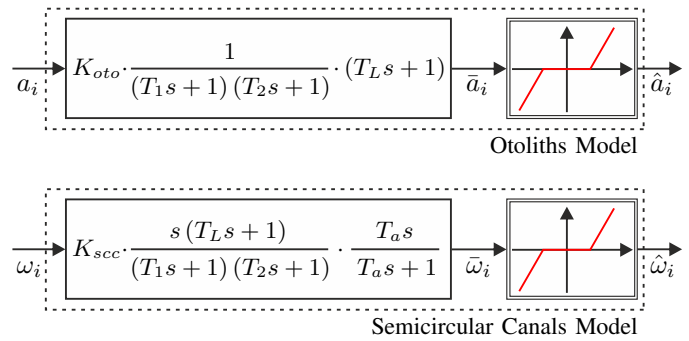


Figure 15. Applied Models of the Vestibular Organs.

filter behavior. Analogous to the semicircular canals model, the passband is found at frequencies of 0.05 to 3 Hz, in which the perceived accelerations \bar{a} at the transfer function outputs contain only a slight amplitude attenuation and phase shift. Thus, the otoliths provide very good acceleration sensors in the frequency range of common driving maneuvers so that translational vehicle movements can be precisely detected. However, low-frequency acceleration stimuli below 0.05 Hz are only perceived with an amplitude attenuated by about -8 dB. In the high-frequency range, a characteristic low-pass behavior is observed, which is due to the inertia of the otoliths. As a consequence, accelerations above 20 Hz, e.g., high-frequency engine vibrations, are only sensed inaccurately by the vestibular organs, so that further perception systems are required for a correct interpretation of the actual motion.

By a series connection of the transfer functions with nonlinear dead zones (see Figure 15), the threshold values $a_{i,thres}$ and $\omega_{i,thres}$ of the human perception are integrated

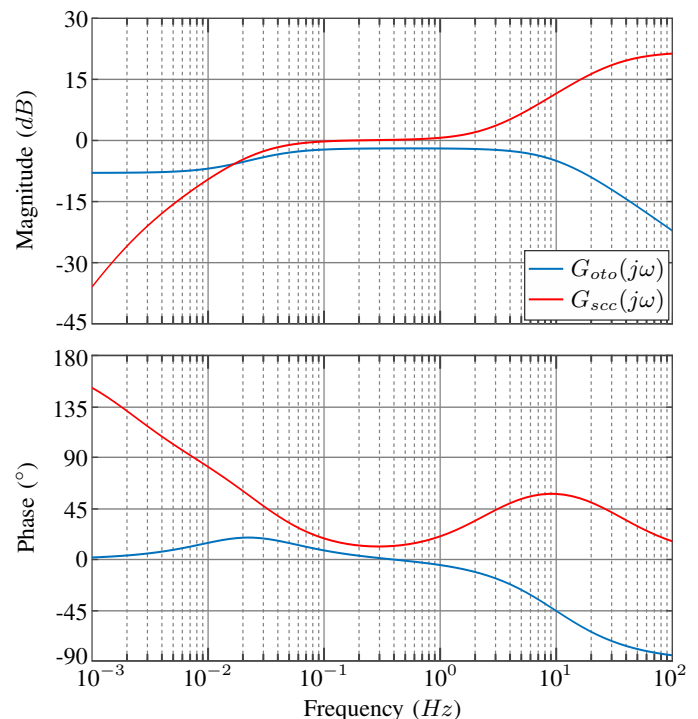


Figure 16. Frequency Responses of the Applied Transfer Function Models.

with respect to the following relationship [8]:

$$\hat{a}_i = \begin{cases} 0 & \text{if } |\bar{a}_i| \leq a_{i,thres} \\ \bar{a}_i - \text{sgn}(\bar{a}_i) \cdot a_{i,thres} & \text{if } |\bar{a}_i| > a_{i,thres} \end{cases} \quad (38)$$

$$\hat{\omega}_i = \begin{cases} 0 & \text{if } |\bar{\omega}_i| \leq \omega_{i,thres} \\ \bar{\omega}_i - \text{sgn}(\bar{\omega}_i) \cdot \omega_{i,thres} & \text{if } |\bar{\omega}_i| > \omega_{i,thres} \end{cases}$$

Consequently, the closer the performance indicators λ_1 and λ_2 are to the origin, the better is the reproduction of the simulated vehicle movements, whereby the value zero indicates a perfect motion rendering. However, especially with regard to λ_1 , this is only a theoretical value that cannot be obtained by any driving simulator, since it would require an almost unlimited workspace.

B. Driving Scenarios

For the purpose of obtaining a representative comparison of the two control strategies, a selection of nine driving scenarios was defined. These contain standardized maneuvers, which are commonly used for development and optimization applications in the automotive industry, like:

- Acceleration from standstill
- Braking from driving straight forward (DIN ISO 70028)
- Lane change (DIN ISO 3888-1)
- Step steering (DIN ISO 7401)
- Braking from steady-state circular course drive (DIN ISO 7975)

As the listed maneuvers are mainly used to identify and analyze the driving dynamics of a vehicle, they do not represent usual driving situations. For this reason, also moderate scenarios are examined in the evaluation:

- Turning at a junction
- Drive on a rural road
- Drive through a roundabout
- Drive through a highway interchange

Vehicle dynamics simulations of all nine maneuvers were performed and the relevant accelerations and angular velocities were recorded. Subsequently, these data were used as identical reference signals for both MCA to ensure a consistent basis for evaluation described in the next section.

VI. RESULTS AND DISCUSSION

Subsequently, the results of the comparison of the two Motion Cueing strategies are presented and the impacts on the interactive driving simulation are discussed. For that purpose, both control algorithms were implemented on the ATMOS driving simulator. Measurement data of the translational accelerations and the angular velocities taken with the installed IMU at the driver's head position serve as inputs for the quality criteria presented in Section V. For reasons of clarity, only the measured data of one driving scenario from each maneuver class are analyzed in detail. All further scenarios will be summarized in the following.

A. Scenario Acceleration from Standstill

First the maneuver "acceleration from standstill" is discussed, in which the simulated vehicle accelerates from standstill to a given speed of 130 km/h. Thereby no steering movements of the driver take place, so that there is no lateral vehicle excitation. Figure 17 shows the resulting longitudinal acceleration and pitch velocity tracking using both MCA. It becomes clear that an adequate reproduction quality of the longitudinal acceleration from the vehicle dynamics simulation is achieved regardless of the applied algorithm. Only when the reference rises rapidly at time $t = 4$ s, there are significant deviations between the simulated and measured acceleration in the driving simulator. In case of the washout algorithm, these can be explained by the signal processing of the washout filters that are used to move the motion system back to the neutral position. At the same time, the tilt coordination rotation is restricted to the delayed dynamics of the low-pass filters, resulting in the illustrated control error. The MPC approach, in contrast, achieves notably smaller deviations. Nevertheless, even with this algorithm, the simulated vehicle acceleration cannot be reproduced exactly, which can be attributed to the limited pitch velocity. As explained in Section IV, the overall rotation rate error of the motion system is bounded to the value of $\varepsilon = 0.1 \text{ rad/s}$ so that unexpected rotations caused by the tilt coordination technique and the kinematic couplings of the motion platform are not perceived disturbingly by the driver [35]. Thus, acceleration deviations, as shown at time $t = 4$ s, are allowed by the optimization algorithm to keep the rotations of the motion system below the perception threshold of the vestibular organs. Without this rotation rate limitation or when using a motion system without couplings between translational and rotational DOF, such as a hexapod, the simulated vehicles acceleration could be reproduced almost exactly in the simulator. In addition, the measured pitch

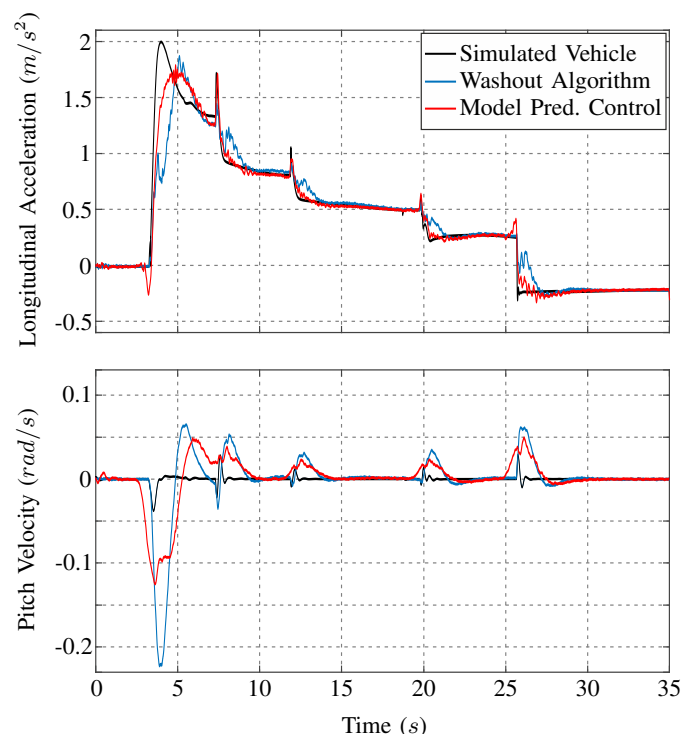


Figure 17. Longitudinal Acceleration and Pitch Velocity Tracking.

velocity in Figure 17 contains in both cases low-frequency disturbances to the vehicle reference resulting from the tilt coordination technique and the forced rotations of the motion platform. When using the filter-based MCA, these deviations are approximately twice as large at the moment of acceleration increase as with the model predictive controller, so that it is to be expected that they have a negative impact on the resulting driving impression. In Figure 18 the lateral acceleration and the corresponding roll velocity tracking are illustrated. As there are no steering actions in this maneuver, the reference values are zero throughout the observed time range. Accordingly, the measured accelerations also provide values close to zero, with only minor deviations due to measurement inaccuracies. However, these are far below the perception threshold and are therefore not noticeable for the driver. Since each translational movement of the motion platform simultaneously causes a vertical displacement of the platform center point, the measured accelerations in Figure 19 contain unpreventable low-frequency errors compared to simulated vehicle acceleration. Due to the available model knowledge, the optimization-based MCA plans the motion trajectory of the simulator in such a way that these deviations are kept below the perception threshold of the otoliths. Furthermore, additionally acting vertical acceleration references, such as at time $t = 26\text{ s}$, are reproduced with high control quality. On the other hand, the washout algorithm generates clearly higher vertical accelerations, since like in the Classical Washout Algorithm, the translational degrees of freedom are considered independently of each other in this approach. Based on these measurement results, the application of the introduced quality criteria provides performance indicators of $\lambda_{1,WO} = 0.68$ and $\lambda_{2,WO} = 0.35$ for the washout algorithm and $\lambda_{1,MPC} = 0.48$ as well as $\lambda_{2,MPC} = 0.18$ for the predictive controller. This objectification confirms the assumption that a higher quality of motion rendering can be achieved using the optimization-based

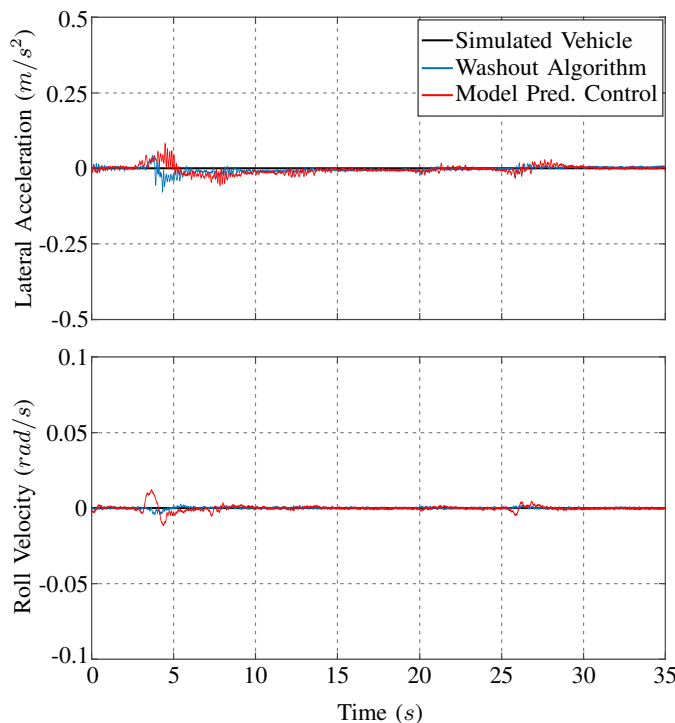


Figure 18. Lateral Acceleration and Roll Velocity Tracking.

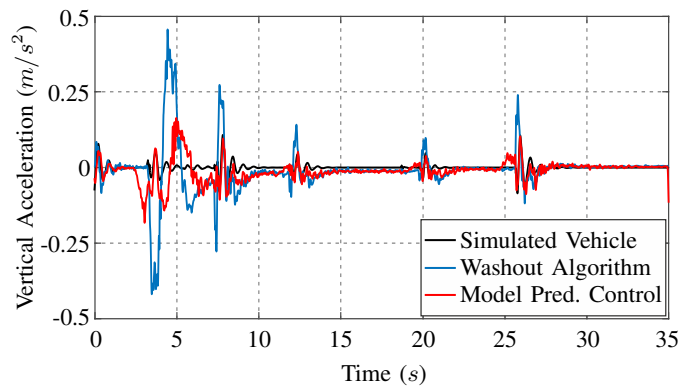


Figure 19. Vertical Acceleration Tracking.

MCA as smaller performance indicators are obtained. An explanation for these results can be found in a more efficient coordination of the motion platform and the shaker system by the MPC. To illustrate this in more detail, Figure 20 shows the actuating variables determined by both approaches during the experiment. Here it can be seen that the actuator reference angles ψ_{ref} in the longitudinal and lateral direction of the motion platform as well as the three shaker actuators located on the left, the right and at the rear remain always within the simulator workspace limitations. However, also the generally different functioning of the two control strategies becomes

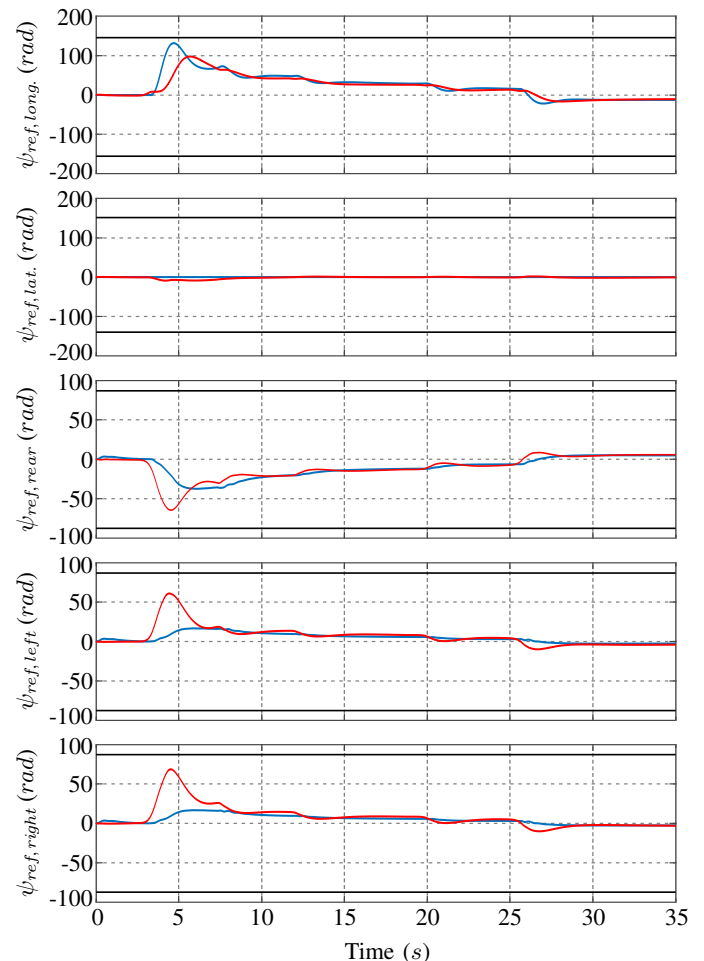


Figure 20. Comparison of the Actuating Variables: Limitation (—), Washout Algorithm (—), Model Predictive Control (—).

clear. While the coordination between motion platform and shaker in the filter-based algorithm is mainly predefined via the static filter parameters and the distribution coefficients, both subsystems are controlled by the MPC according to the current driving situation and the actual state of the motion system. For this reason, there is a variable distribution between motion platform and shaker in each driving scenario. Both systems are thereby used asynchronously in order not to exceed the rotation rate limitation due to the coupled DOF and the nonlinear kinematics of the motion system, as can be observed at time $t = 4$ s. In addition, there is a better exploitation of the available workspace by the model predictive control algorithm.

B. Scenario Turning at a Junction

As an example of an everyday driving situation, the scenario “turning at a junction” with simultaneously acting longitudinal and lateral acceleration references will be examined subsequently. In contrast to the previously discussed maneuver, the reproduction of lateral accelerations using the presented Motion Cueing strategies can thus also be analyzed. Figure 21 illustrates the tracking of the simulated vehicles longitudinal acceleration and pitch velocity. Again it becomes clear that both the washout algorithm and the optimization-based MCA yield an adequate reproduction of the longitudinal acceleration. However, the measured accelerations show, such as at time $t = 10$ s, a larger delay in comparison to the reference signal when using the washout algorithm due to the phase shift of the implemented filters. Also in this maneuver, the associated pitch velocity contains in both cases low-frequency disturbances that can be explained by the tilt coordination, since sustained acceleration components can only be reproduced by an equivalent rotation of the motion system. Using the washout algorithm, these errors are significantly higher due to the forced rotation of the motion platform, so it can be expected that the resulting driving experience will

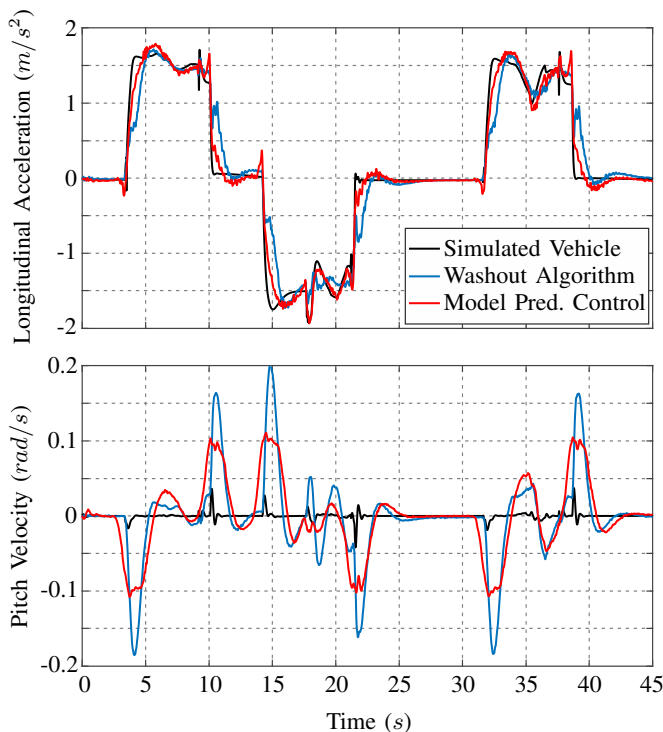


Figure 21. Longitudinal Acceleration and Pitch Velocity Tracking.

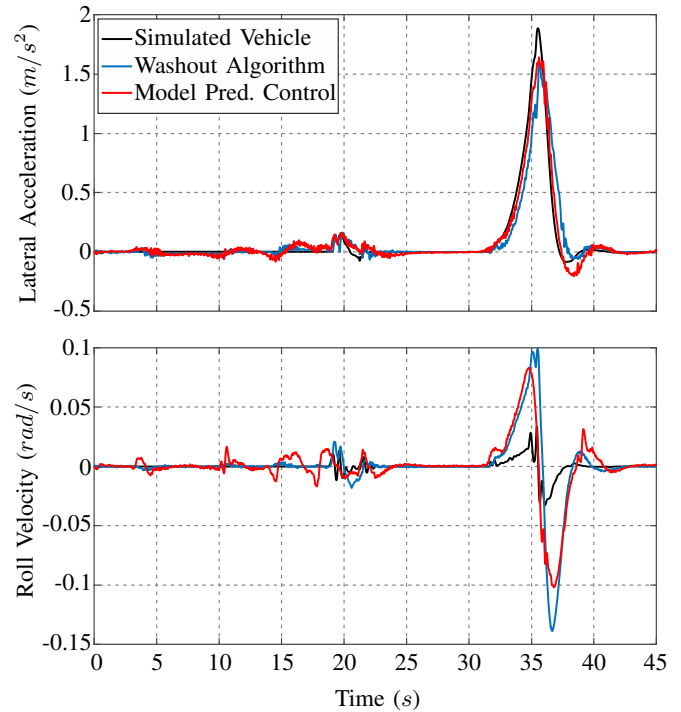


Figure 22. Lateral Acceleration and Roll Velocity Tracking.

be negatively affected. In contrast, the predictive MCA uses the integrated kinematics information to successfully limit the overall rotation rate error to 0.1 rad/s . As a result of this limitation, minor errors in the tracking of the acceleration reference occur, which are more difficult to detect by the driver in the simulator than unexpected strong rotations. Equivalent results can be derived from Figure 22, that illustrates the lateral acceleration and the corresponding roll velocity. As shown, the acceleration reference from the vehicle dynamics simulation is tracked very well with both algorithms. There are again time delays to the reference signal that are larger when using the washout algorithm, resulting from the phase shift of the implemented filters. The roll velocity error is also larger compared to the MPC, even if the difference between both algorithms is smaller than in case of the pitch velocity. Thus, as a consequence for the interactive driving simulation, the resulting driving experience can be expected to be more realistic using the predictive control strategy, since smaller rotation rate errors are more difficult to detect for the human perception system. The vertical acceleration measured in the examined driving scenario is illustrated in Figure 23. Also in this maneuver it is noticeable that due to the coupled DOF of the motion system, undesired vertical displacements occur, which cannot be fully compensated by either control strategy. However, these errors are significantly lower and mostly below the human perception threshold in the use of the predictive MCA. The washout algorithm, on the other hand, generates detectable sensory conflicts since no interactions between horizontal and vertical accelerations are considered in the underlying algorithm structure. To objectify these findings, the quality criteria introduced in the previous section are used, resulting in performance indicators $\lambda_{1,WO} = 1.74$ and $\lambda_{2,WO} = 0.92$ for the washout algorithm and $\lambda_{1,MPC} = 1.20$ and $\lambda_{2,MPC} = 0.53$ for the optimization-based MCA. It becomes consequently clear that a higher control quality is achieved with the MPC, which is primarily explained by the

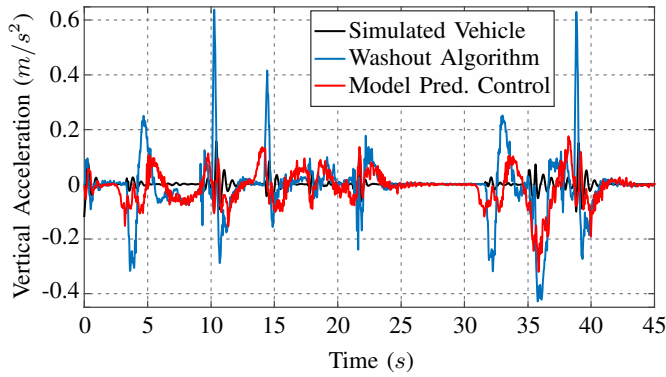


Figure 23. Vertical Acceleration Tracking.

lower angular velocity and vertical acceleration errors caused by the specific kinematics of the ATMOS driving simulator. Here, the differences between filter-based and optimization-based MCA are again obvious when considering the associated actuating variables in Figure 24. Although both algorithms respect the available workspace of the installed actuators at all times, the coordination of the motion platform and the shaker system shows significant differences. Similar to the example of the previously considered driving scenario, the shaker is used more in the model predictive algorithm in order to compensate the coupling effects of the motion platform best

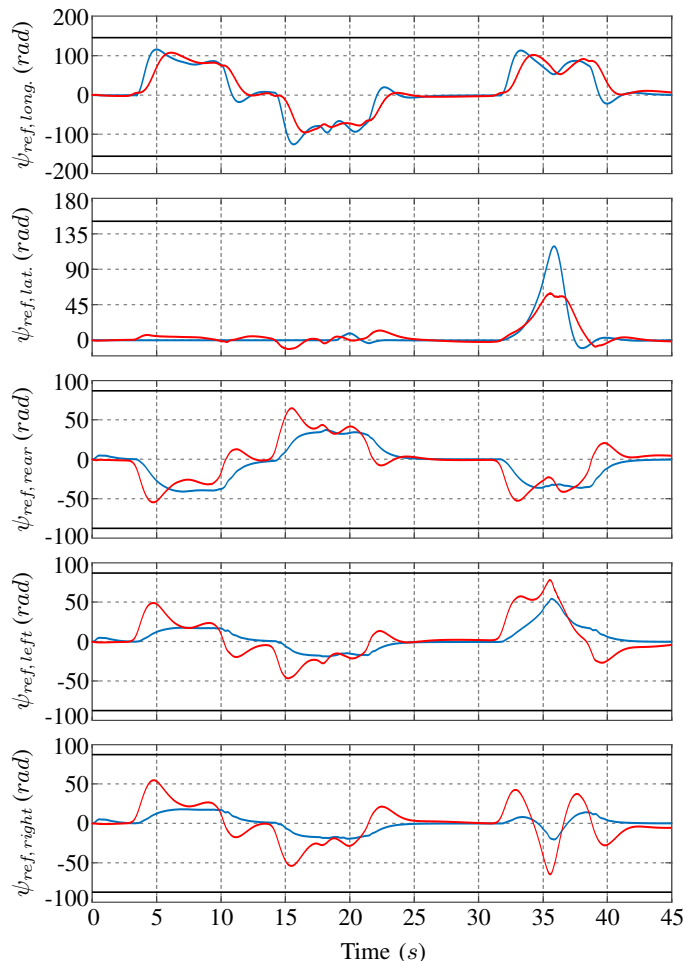


Figure 24. Comparison of the Actuating Variables: Limitation (-), Washout Algorithm (-), Model Predictive Control (-).

possible. Thereby, the motion trajectories of both subsystems are planned asynchronously (see e.g., at time $t = 10$ s) to comply with the given rotation rate limitations of 0.1 rad/s while reproducing the acceleration references from the simulated vehicle. In the washout algorithm, in contrast, there are no compensation operations with the shaker, resulting in the rotation rate and vertical acceleration errors illustrated in the Figures 21, 22 and 23.

C. Summarized Evaluation of all Driving Scenarios

The evaluation process described before using the example of two selected driving maneuvers was performed for all nine test scenarios in the context of this paper. Thereby, the performance indicators listed in Table II were obtained. A graphical analysis of these results can be seen in Figure 25, which combines the evaluation of all maneuvers in a common radar chart. Here, the two driving scenarios “acceleration from standstill” and “turning at a junction” exhibit the lowest and the highest performance indicators respectively. But it should be noted that the individual maneuvers are not comparable with each other, as they differ significantly in terms of the underlying driving dynamics. For example, purely longitudinal scenarios such as “braking from driving straight forward” naturally generate lower values of λ_1 and λ_2 than more challenging maneuvers with simultaneously acting longitudinal and lateral accelerations. However, the presented evaluation framework enables a reliable objective comparison of both Motion Cueing strategies for each separate driving scenario. The chart clearly shows the advantages of the optimization-based MCA in comparison to the washout algorithm, since smaller performance indicators are achieved in each of the examined scenarios. Here, it is noticeable that the perceived control quality, expressed by the indicator λ_2 , yields small values close to zero when the MPC is used and therefore a good subjective driving impression can be expected. As already discussed in detail in the previous sections, these results can be explained with the angular velocity and vertical acceleration errors due to the coupled degrees of freedom, because of which an adequate reproduction of the simulated vehicles Motion Cues is a challenging task. Here, it is a great advantage of the MPC that the specific simulator kinematics are directly considered via existing model knowledge in the optimization algorithm. This allows undesired interactions to be taken into account in the planning of the motion trajectory and optimally compensated according to the current driving situation, which is a major benefit for interactive driving simulation.

TABLE II. DETERMINED PERFORMANCE INDICATORS.

Driving Scenario	$\lambda_{1,WO}$	$\lambda_{2,WO}$	$\lambda_{1,MPC}$	$\lambda_{2,MPC}$
Acceleration from Standstill	0.68	0.35	0.48	0.18
Braking from Driving Straight Forward	0.53	0.25	0.39	0.14
Lane Change	1.77	0.99	1.12	0.51
Step Steering	1.38	0.98	0.67	0.36
Braking from Steady-State	0.91	0.40	0.62	0.20
Circular Course Drive				
Turning at Junction	1.74	0.92	1.20	0.53
Drive Through Rural Road	1.19	0.60	0.81	0.30
Drive Through Roundabout	1.47	0.80	0.96	0.41
Drive Through Highway Interchange	0.96	0.42	0.58	0.19

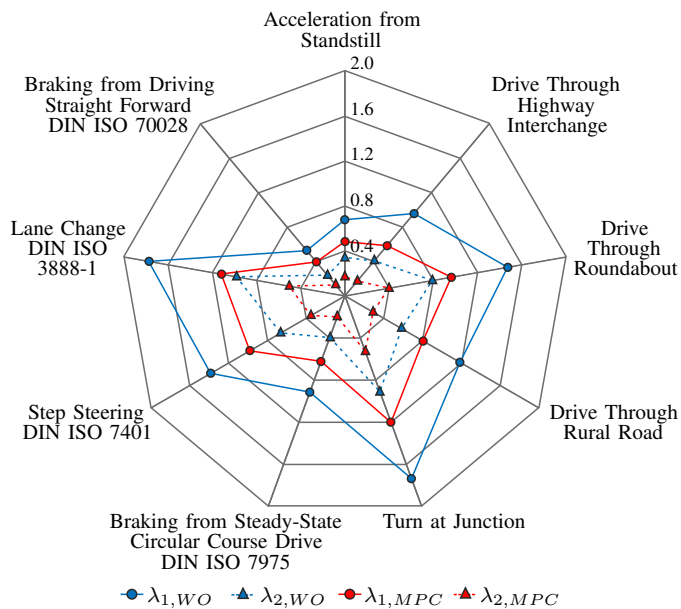


Figure 25. Evaluation of the Analyzed Test Maneuvers.

VII. CONCLUSION AND FUTURE WORK

In this paper, the development of different Motion Cueing Algorithms for a hybrid kinematics driving simulator with 5 degrees of freedom was presented. Motivated by the unique characteristics of the considered motion system, a comprehensive extension of the filter-based Classical Washout Algorithm was designed first. Key features of the resulting control strategy form a dynamic position washout to any point within the simulator workspace, as well as a tilt coordination distribution strategy in order to make full use of the motion capabilities. However, similar to the basic idea of the CWA, this approach does not consider couplings between the individual translational DOF, which leads to undesired interdependencies that may disturb the driving impression under certain circumstances. To overcome this, an optimization-based MCA using the concept of Model Predictive Control was implemented. It includes a simplified model of the controlled actuators as well as the nonlinear kinematic relations of the motion system to optimally plan the trajectory of the simulator in real-time, taking into account given constraints. Thus, the physical limits of the system, such as the restricted workspace, are respected and the occurring coupling effects are compensated best possible.

To analyze the resulting control quality, both algorithms were objectively compared by means of defined quality criteria and standard driving scenarios from the automotive industry. Thereby, a satisfactory motion rendering was proven for each Motion Cueing strategy. However, due to the integration of model knowledge, the predictive MCA exhibits less control errors in angular velocities and vertical acceleration. For this reason, it is assumed that the subjective driving impression is more realistic when using the MPC, which is why this approach offers great potential for interactive driving simulation. On the other hand, the filter-based MCA has the advantages of simple implementation, good traceability and low computational effort, which relativizes the worse control quality in comparison to the optimization-based algorithm.

The future work will deal with the subjective validation of

our observations. In this context, reliable subject studies will be conducted in order to rate the resulting degree of immersion by human Drivers-in-the-Loop. Thus, it will be possible to investigate by paired comparison of both approaches whether there is a correlation between the perceived control performance and the objective results presented in this paper. In addition, methods from the field of decoupling control theory can be integrated in the modified washout algorithm to compensate the vertical movements of the motion platform with the shaker in a limited area of the workspace, so that occurring False Cues are reduced more effectively.

REFERENCES

- [1] P. Biemelt, S. Mertin, N. Rüdtenklau, S. Gausemeier, and A. Trächtler, "Objective Evaluation of a Novel Filter-Based Motion Cueing Algorithm in Comparison to Optimization-Based Control in Interactive Driving Simulation," 11th International Conference on Advances in System Simulation (SIMUL), 2019, pp. 25–31.
- [2] N. Rüdtenklau, P. Biemelt, S. Henning, S. Gausemeier, and A. Trächtler, "Real-Time Lighting of High-Definition Headlamps for Night Driving Simulation," International Journal On Advances in Systems and Measurements, vol. 12, 2019, pp. 72–88.
- [3] V. Melcher, S. Rauh, F. Diederichs, H. Widloirther, and W. Bauer, "Take-Over Requests for automated driving," Procedia Manufacturing, vol. 3, 2015, pp. 2867–2873.
- [4] H. Bellem et al., "Can We Study Autonomous Driving Comfort in Moving-Base Driving Simulators? A Validation Study," Human Factors, vol. 59, no. 3, 2017, pp. 442–456.
- [5] T. Murano, T. Yonekawa, M. Aga, and S. Nagiri, "Development of High-Performance Driving Simulator," SAE International Journal of Passenger Cars-Mechanical Systems, vol. 2, 2009, pp. 661–669.
- [6] E. Zeeb, "Daimler's New Full-Scale, High-dynamic Driving Simulator – A Technical Overview," Driving Simulation Conference Europe (DSC), 2010, pp. 157–165.
- [7] S. F. Schmidt and B. Conrad, "Motion Drive Signals for Piloted Flight Simulators," I Contract Report NASA, CR-1601, 1970.
- [8] L. D. Reid and M. A. Nahon, "Flight Simulation Motion-Base Drive Algorithms: Part 1 - Developing and Testing the Equations," University of Toronto, UTIAS Report 296, 1985.
- [9] T. Sammet, "Motion-Cueing-Algorithmen für die Fahrsimulation (Motion Cueing Algorithms for Driving Simulation)," Fortschritt Berichte-VDI Reihe 12 Verkehrstechnik/Fahrzeugtechnik, vol. 643, 2007.
- [10] K. Patil, S. K. Molla, and T. Schulze, "Hybrid Vehicle Model Development using ASM-AMESim-Simscape Co-Simulation for Real-Time HIL Applications," SAE Technical Paper, Tech. Rep., 2012.
- [11] D. Stewart, "A Platform with Six Degrees of Freedom," Proceedings of the Institution of Mechanical Engineers, vol. 180, no. 1, 1965, pp. 371–386.
- [12] G. Bertolini and D. Straumann, "Moving in a Moving World: A Review on Vestibular Motion Sickness," Frontiers in Neurology, vol. 7, no. 14, 2016.
- [13] P. Biemelt, S. Mertin, N. Rüdtenklau, S. Gausemeier, and A. Trächtler, "Design and Evaluation of a Novel Filter-Based Motion Cueing Strategy for a Hybrid Kinematics Driving Simulator with 5 Degrees of Freedom," Driving Simulation Conference Europe (DSC), 2020.
- [14] M. Bruschetta, F. Maran, and A. Beghi, "A fast implementation of MPC-based motion cueing algorithms for mid-size road vehicle motion simulators," Vehicle System Dynamics, vol. 55, no. 6, 2017, pp. 802–826.
- [15] J. O. Pitz, "Vorausschauender Motion-Cueing-Algorithmus für den Stuttgarter Fahr Simulator (Predictive Motion Cueing Algorithm for the Stuttgart Driving Simulator)," PhD Thesis, Universität Stuttgart, 2017.
- [16] P. Biemelt, S. Henning, N. Rüdtenklau, S. Gausemeier, and A. Trächtler, "A Model Predictive Motion Cueing Strategy for a 5-Degree-of-Freedom Driving Simulator with Hybrid Kinematics," Driving Simulation Conference Europe (DSC), 2018, pp. 79–85.
- [17] J. Richalet and D. O'Donovan, Predictive Functional Control: Principles and Industrial Applications. Springer Science & Business Media, 2009.

- [18] A. J. Benson, E. C. Hutt, and S. F. Brown, "Thresholds for the Perception of Whole Body Angular Movement about a Vertical Axis," *Aviation, Space, and Environmental Medicine*, vol. 60, 1989, pp. 205–213.
- [19] N. Wiener, "Nonlinear Problems in Random Theory," MIT Press, Cambridge, 1958.
- [20] J. M. Maciejowski, "Predictive Control with Constraints," Pearson Education, 2002.
- [21] O. Föllinger, "Regelungstechnik: Einführung in die Methoden und ihre Anwendung (Control Engineering: Introduction to the Methods and their Application)," VDE Verlag, 2013.
- [22] M. Katliar, K. N. De Winkel, J. Venrooij, P. Pretto, and H. H. Bühlhoff, "Impact of MPC Prediction Horizon on Motion Cueing Fidelity," *Driving Simulation Conference Europe (DSC)*, 2015, pp. 219–222.
- [23] M. Grottole, D. Cleij, P. Pretto, Y. Lemmens, R. Happee, and H. H. Bühlhoff, "Objective evaluation of prediction strategies for optimization-based motion cueing," *Simulation: Transactions of the Society for Modeling and Simulation International*, vol. 95, no. 8, 2018, pp. 707–724.
- [24] P. Biemelt, C. Link, S. Gausemeier, and A. Trächtler, "A Model-Based Online Reference Prediction Strategy for Model Predictive Motion Cueing Algorithms," *21st IFAC World Congress*, 2020.
- [25] K. Svanberg, "A Class of Globally Convergent Optimization Methods Based on Conservative Convex Separable Approximations," *SIAM Journal on Optimization*, vol. 12, no. 2, 2002, pp. 555–573.
- [26] S. G. Johnson, "The NLOpt nonlinear-optimization package," <https://nlopt.readthedocs.io/en/latest/>, last call December 7th 2020.
- [27] D. G. Luenberger, "Observing the State of a Linear System," *IEEE Transactions on Military Electronics*, vol. 8, no. 2, 1964, pp. 74–80.
- [28] N. A. Pouliot, C. M. Gosselin, and M. A. Nahon, "Motion Simulation Capabilities of Three-Degree-of-Freedom Flight Simulators," *Journal of Aircraft*, vol. 35, no. 1, 1998, pp. 9–17.
- [29] I. Al Qaisi and A. Trächtler, "Human in the Loop: Optimal Control of Driving Simulators and New Motion Quality Criterion," *IEEE International Conference on Systems, Man, and Cybernetics (SMC)*, 2012, pp. 2235–2240.
- [30] P. Grant, M. Blommer, B. Artz, and J. Greenberg, "Analysing Classes of Motion Drive Algorithms Based on Paired Comparison Techniques," *Vehicle System Dynamics*, vol. 47, no. 9, 2009, pp. 1075–1093.
- [31] A. Siegel and H. N. Sapru, *Essential Neuroscience*. Lippincott Williams & Wilkins, 2006.
- [32] L. R. Young and J. L. Meiry, "A Revised Dynamic Otolith Model," *Aerospace Medicine*, vol. 39, no. 6, 1968, pp. 606–608.
- [33] C. Fernandez and J. M. Goldberg, "Physiology of Peripheral Neurons Innervating Semicircular Canals of the Squirrel Monkey. II. Response to Sinusoidal Stimulation and Dynamics of Peripheral Vestibular System," *Journal of Neurophysiology*, vol. 34, no. 4, 1971, pp. 661–675.
- [34] R. J. Telban and F. M. Cardullo, "Motion Cueing Algorithm Development: Human-Centered Linear and Nonlinear Approaches," *National Aeronautics and Space Administration (NASA), CR-2005-213747, Tech. Rep.*, 2005.
- [35] A. Nesti, C. Masone, M. Barnett-Cowan, P. Robuffo Giordano, H. H. Bühlhoff, and P. Pretto, "Roll rate thresholds and perceived realism in driving simulation," *Driving Simulation Conference Europe (DSC)*, 2012, pp. 23–31.